The Astrophysical Journal, 704:1021–1035, 2009 October 20 doi:10.1088/0004-637X/704/2/1021

SOLAR CYCLE VARIATIONS OF CORONAL NULL POINTS: IMPLICATIONS FOR THE MAGNETIC BREAKOUT MODEL OF CORONAL MASS EJECTIONS

G. R. Cook[1], D. H. Mackay[1], and Dibyendu Nandy[2]
[1] School of Mathematics and Statistics, North Haugh, University of St Andrews, St Andrews, Fife, KY16 9SS, Scotland; graeme@mcs.st-and.ac.uk, duncan@mcs.st-and.ac.uk
[2] Indian Institute of Science Education and Research, Kolkata, India; dnandi@iiserkol.ac.in
Received 2009 May 14; accepted 2009 September 8; published 2009 September 25

ABSTRACT

In this paper, we investigate the solar cycle variation of coronal null points and magnetic breakout configurations in spherical geometry, using a combination of magnetic flux transport and potential field source surface models. Within the simulations, a total of 2843 coronal null points and breakout configurations are found over two solar cycles. It is found that the number of coronal nulls present at any time varies cyclically throughout the solar cycle, in phase with the flux emergence rate. At cycle maximum, peak values of 15–17 coronal nulls per day are found. No significant variation in the number of nulls is found from the rising to the declining phase. This indicates that the magnetic breakout model is applicable throughout both phases of the solar cycle. In addition, it is shown that when the simulations are used to construct synoptic data sets, such as those produced by Kitt Peak, the number of coronal nulls drops by a factor of 1/6. The vast majority of the coronal nulls are found to lie above the active latitudes and are the result of the complex nature of the underlying active region fields. Only 8% of the coronal nulls are found to be connected to the global dipole. Another interesting feature is that 18% of coronal nulls are found to lie above the equator due to cross-equatorial interactions between bipoles lying in the northern and southern hemispheres. As the majority of coronal nulls form above active latitudes, their average radial extent is found to be in the low corona below 1.25 $R_{\odot}$ (175,000 km above the photosphere). Through considering the underlying photospheric flux, it is found that 71% of coronal nulls are produced though quadrupolar flux distributions resulting from bipoles in the same hemisphere interacting. When the number of coronal nulls present in each rotation is compared to the number of bipoles emerging, a wide scatter is found. The ratio of coronal nulls to emerging bipoles is found to be approximately 1/3. Overall, the spatio-temporal evolution of coronal nulls is found to follow the typical solar butterfly diagram and is in qualitative agreement with the observed time dependence of coronal mass ejection source-region locations.

Key words: Sun: activity – Sun: corona – Sun: coronal mass ejections (CMEs) – Sun: magnetic fields

1. INTRODUCTION

The study of coronal null points, locations where $\mathbf{B} = \mathbf{0}$ in the solar atmosphere, is currently a key area of research in solar physics. Null points are of interest as they are sites where magnetic reconnection—accompanied by energy release—can take place within the solar atmosphere (Pontin et al. 2004; Aulanier et al. 2005; Pariat et al. 2006; Priest et al. 2003). The properties and existence of coronal null points depend on the complex nature of the magnetic field distribution at the solar photosphere. This distribution may be mathematically prescribed as a boundary condition in magnetic field extrapolation techniques. Many studies have considered the existence and properties of coronal null points either through considering theoretical configurations (Brown & Priest 1999, 2001; Parnell et al. 1996, 1997; Beveridge et al. 2002, 2004; Parnell & Galsgaard 2004; Parnell et al. 2008) or through direct extrapolation of observed magnetograms (Longcope et al. 2003; Démoulin 2005; Maclean et al. 2005; Démoulin 2006; Régnier et al. 2008; Longcope & Beveridge 2007; Longcope & Parnell 2009). To date, most of these studies of coronal null points have been carried out under the potential field approximation and in a local cartesian frame of reference. A few studies have also considered the existence of coronal null points in spherical geometry due to a few sources (Maclean et al. 2006a, 2006b; Maclean & Priest 2007) or in non-potential magnetic field distributions.

In the paper of Antiochos (1998; see also Antiochos et al. 1999; MacNeice et al. 2004; Lynch et al. 2004; Choe et al. 2005), a coronal null point plays a key role in the escape of coronal mass ejections (CMEs) from the Sun, in what is called the *magnetic breakout model*. A CME is a violent ejection of plasma, which may be directed earthward with disastrous consequences. The key features of the magnetic breakout model as set up by Antiochos (1998) can be seen in Figure 1(a). The initial configuration consists of a quadrupolar photospheric flux distribution and an overlying potential field. Even with such a simple photospheric distribution, the resulting coronal field has four distinct flux domains. The field lines within the two domains which pass over the equator are oppositely orientated to one another. Between them lies a coronal null point. This coronal null point is a key feature; when the field underneath it is stressed, reconnection may occur allowing the underlying flux to break out. While in a two-dimensional situation a null point is required for reconnection to occur, in a three-dimensional situation, reconnection may also occur at other locations without nulls such as current sheets (Priest & Démoulin 1995; Démoulin et al. 1996; Hornig & Priest 2003; Titov et al. 2003; Galsgaard et al. 2003; Pontin et al. 2005; Haynes et al. 2007). For simplicity, the focus of this study is the variation of coronal null points as they are a mathematically (and numerically) identifiable topological feature and a key element in the initial configuration of breakout topologies as described by Antiochos (1998). Thus, the variation of these null points will indicate the variation of possible breakout topologies and CMEs associated with them.

A key aspect of coronal null points and the breakout model, which is tested here, is their dependence on the solar cycle phase. This is illustrated in Figures 1(b) and (c), which give possible

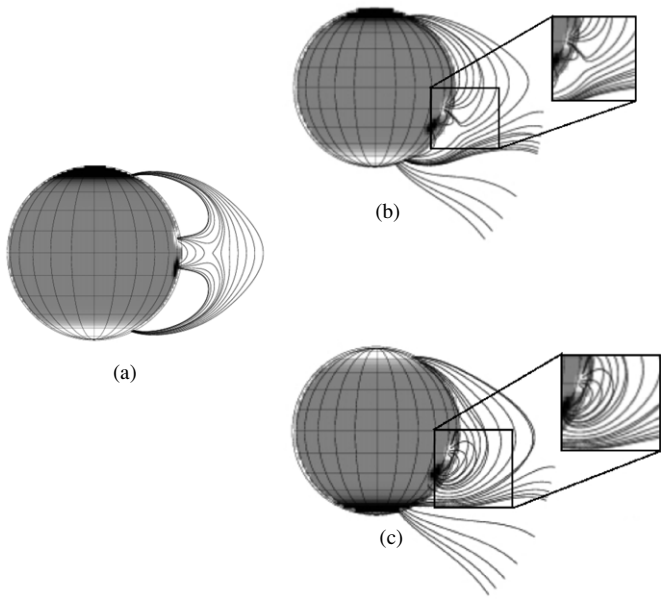

Figure 1. (a) Initial setup of the breakout model. The setup consists of a quadrupolar photospheric field (white ∼ positive flux, black ∼ negative flux) with extrapolated overlying potential field denoted by the field lines which are plotted in a single radial plane. The dipole orientation of the equatorial regions of flux are opposite to that of the polar regions, resulting in a coronal null point whose location is denoted by the X-point structure in the field. (b) Example showing the field setup with one bipole inserted before global dipole reversal and (c) after global dipole reversal. In (b), the two oppositely orientated central flux regions will cause a coronal null point to form above the bipole, whereas, in (c) no coronal null point will form due to the central regions being of the same orientation.

flux distributions in the rising (before global dipole reversal) and declining (after global dipole reversal) phases of the solar cycle. For both of these cases, the magnetic distributions represent those likely to occur on the Sun, as opposed to the idealized case depicted in Figure 1(a). Before global dipole reversal, it can clearly be seen that the overlying dipole field is of opposite orientation to the underlying field caused by the bipolar region. This means that a coronal null point and a magnetic breakout configuration exist. However, after global dipole reversal the overlying field is of the same orientation as the underlying field caused by the bipolar region. No coronal null point occurs (instead two photospheric null points occur between the two negative polarities and the two positive polarities). This raises two very important questions: (1) Do coronal null points and magnetic breakout configurations occur during the declining phase of the cycle and is there a cycle phase dependence in their occurrence? and (2) If null points and breakout configurations do occur in the declining phase what causes their existence if not the global dipole? It should also be noted that other models exist for the initiation of a CME where these do not require coronal null points. These include varying processes such as flux injection (Chen 1989, 1996), flux cancellation (van Ballegooijen & Martens 1989; Priest & Forbes 1990; Forbes & Priest 1995), and dynamical instabilities (Tokman & Bellan 2002; Török & Kliem 2003; Kusano et al. 2004). Recently, Yeates & Mackay (2009) carried out global simulations of the coronal field based on observed magnetograms and found that flux cancellation leading to the formation and loss of equilibrium of flux ropes could account for 50% of the observed CME rates for a six month period in 1999. For a review on CME mechanisms see the papers of Klimchuk (2001) and Lin et al. (2003).

In a previous study, Barnes (2007) compared CME locations with the occurrence of null points in an effort to deduce whether the breakout model could account for observed eruptions. In this work, 1800 vector magnetograms were subjected to a magnetic charge topology analysis, and the null points were determined. It was found that while there was a strong statistical correlation between at least one coronal null being present and eruptive events, the majority of events (74%) occur in areas where no coronal null was present. Barnes (2007) concluded that the breakout model cannot be used to explain all of the CMEs that occur. The study of Barnes (2007) is fundamentally different from the work presented in this paper due to the fact that the observations used by Barnes were of a limited field of view. In this paper, the existence of coronal null points and their relevance to magnetic breakout configurations is studied through modeling the global field, including the overlying global dipolar field configuration in spherical geometry. Two discrete but coupled mathematical models are used. The first produces the lower boundary condition representing the radial magnetic field at the solar surface. This is specified though flux transport simulations which self-consistently produce the strength of the global dipole based on the amount of flux emerged at low latitudes and its subsequent evolution through flux transport processes. Two forms of this lower boundary condition are used. The first, which we call the "instant day simulation," produces the radial magnetic field over the entire surface of the Sun at any given instant in time and is produced directly by the output of the flux transport simulations. The second is where we use the output from the instant day simulations to produce "simulated synoptic magnetograms" in a comparable manner to the observed synoptic magnetograms of Kitt Peak (KP). In the context of this study the instant day simulations may be regarded as the true representation of the magnetic field across the entire surface of the Sun, while the simulated synoptic magnetograms are an approximate representation that would occur as a result of only being able to view one side of the Sun at any one time. By doing so, we will determine what information is lost when dealing with the solar synoptic observations. The second component is a potential field source surface (PFSS) model (Schatten et al. 1969) which extrapolates a global coronal magnetic field from the photospheric flux distribution out to 2.5 solar radii. The location and variation of coronal null points within the PFSS is then determined. Through this a better understanding of null point variation throughout the entire global field is found, as opposed to over isolated active regions.

The paper is ordered as follows. The simulation method is described in Section 2. This will include a description of the "instant day" simulation, along with the construction of "simulated synoptic magnetograms." The extrapolation of a potential field out to 2.5 solar radii is also described along with a description of the null point finding technique. Section 3 will discuss the origin, behavior, and variation of coronal null points for both the instant day and simulated synoptic distributions. Finally, Section 4 will present the concluding discussions.

2. THE MODEL

To investigate the solar cycle variation of coronal null points and subsequently magnetic breakout configurations, a mixture of magnetic flux transport and PFSS models are used. A key constraint of these simulations is that the absolute flux values used within the flux transport simulations are matched to levels determined from KP synoptic magnetograms. The techniques

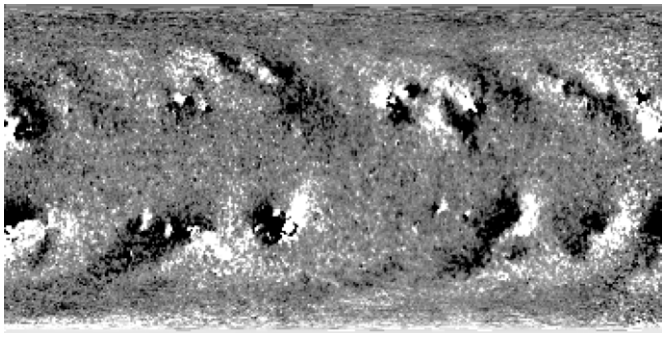

Figure 2. Example of a Kitt Peak synoptic magnetogram. White indicates positive flux and black indicates negative flux where the image is set to saturate at ±10 G.

employed and why observed flux distributions, such as KP synoptic magnetograms, are not directly applied are described next.

2.1. KP Magnetograms

KP synoptic magnetograms represent a monthly average of the Sun's global photospheric field and are created from National Solar Observatory (NSO)/KP normal component full disk magnetograms (Pierce et al. 1976). Each synoptic magnetogram represents one Carrington rotation (27 days) of measurement. An example of a KP magnetogram is given in Figure 2. Synoptic magnetograms have been used for a variety of purposes, including the study of the 27 day period found on the Sun (Henney & Harvey 2001), the study of coronal holes during solar maximum (Zhang et al. 2002), considering the origin of the hemispheric pattern of filaments (Mackay et al. 2000; Yeates et al. 2007, 2008) and in the study of the origin of CMEs (Yeates & Mackay 2009).

One method of investigating the existence of coronal null points could be to use the synoptic magnetograms as a lower boundary condition coupled with the PFSS approximation. However, as previously discussed, the existence of coronal null points may critically depend on the distribution and strength of the polar field and global dipole. Therefore, the direct use of synoptic magnetograms in such a study has two disadvantages. The first is that due to line-of-sight effects, beyond ±60° latitude the polar field measurements are unreliable. Therefore, when using observed magnetograms, synoptic or otherwise, the effect of the global dipole on the underlying flux and coronal null points may not be accurately modeled.

Secondly, due to the method of producing synoptic magnetograms information may be lost. This may occur if a bipole emerges at a longitude after that longitude has passed through central meridian (or if the longitude lies on the far side of the Sun). Such a bipole may be significantly weakened or have completely disappeared by the time the Sun has rotated enough for the relevant field information to be extracted by the next rotation.

As it is difficult to quantify what information is lost, KP synoptic magnetograms are not directly used as a base boundary condition within the simulation. Rather, we prefer to carry out theoretical simulations that accurately represent the surface magnetic field over the whole Sun throughout the solar cycle. In these simulations, to obtain realistic flux distributions, we simulate the emergence of a large number of synthetic magnetic bipoles. The bipoles are assumed to emerge at random longitudes and follow the observed properties of the butterfly diagram in addition to Hale's polarity law and Joy's law. Based on the work of Harvey & Zwaan (1993) and Schrijver & Harvey (1994), the emergence rate of individual bipoles is inversely proportional to the size of regions. The properties of the bipoles are discussed further in Section 2.2.1 and are shown in Figure 3. In order to produce realistic flux distributions as a function of latitude, the emergence rate and properties of the bipoles are varied so that the net flux values in the simulation at low latitudes, match those found in KP data. The subsequent polar field strengths are then self-consistently determined through the surface flux transport processes. Secondly, from these computations, simulated synoptic data are produced—which allow us to quantify what information is lost through producing such data and how this affects the number of coronal nulls. The method of doing this along with the flux transport simulations are discussed in the next section.

2.2. Flux Transport Simulation and Coronal Null Point Identification

There are several steps that must be followed to determine the variation of coronal null points and breakout topologies. First, magnetic flux transport simulations are carried out, where at any instant in time these simulations describe the radial magnetic field ($B_r(\theta, \phi, t)$) across the whole solar surface (Section 2.2.1). These are called the "instant day simulations" as they give the radial distribution of magnetic field across the whole Sun at any instant in time. This simulation may be regarded as the actual representation of the Sun's magnetic field. From this the "simulated synoptic magnetograms" are constructed (Section 2.2.2), where these represent a global approximation to the true field as only one side of the Sun may be observed at any one time. Next, both the "instant day" and "simulated synoptic" data are used as lower boundary conditions for a PFSS model (Section 2.2.3), which extrapolates a magnetic field from the solar surface into a coronal volume. Finally, the numerical null point finding technique of Haynes & Parnell (2007) is used to study the properties of the coronal null points (Section 2.2.4). Full details of each of these stages are now described.

2.2.1. Instant Day Simulations

Magnetic flux at the solar surface evolves through the processes of emergence, advection, and surface diffusion. New flux emerges at the solar surface in the form of newly emerged bipolar regions (Archontis et al. 2004; Murray et al. 2006; Murray & Hood 2007). Once emerged, the flux is evolved via large-scale flows such as differential rotation and meridional flow. The flux transport code used in this study includes these effects along with surface diffusion as a result of super-granular convection in order to evolve the radial component of the magnetic field forward at the solar surface (Wang et al. 1989; van Ballegooijen et al. 1998; Schrijver & Title 2001; Baumann et al. 2006). The evolution of the radial component of the magnetic field at the solar surface ($r = R_\odot = 1$) is given by

$$\frac{\partial \mathrm{B}_r}{\partial \mathrm{t}} = \frac{1}{\sin\theta}\frac{\partial}{\partial\theta}\left(\sin\theta\left(-u(\theta)\mathrm{B}_r + D\frac{\partial \mathrm{B}_r}{\partial\theta}\right)\right) - \Omega(\theta)\frac{\partial \mathrm{B}_r}{\partial\phi} + \frac{D}{\sin^2\theta}\frac{\partial^2 \mathrm{B}_r}{\partial\phi^2}, \quad (1)$$

where $\mathrm{D} = 600\ \mathrm{km^2\ s^{-1}}$ is the diffusion coefficient. The value of D has been taken from previous studies (Wang et al. 1989; van Ballegooijen et al. 1998) where its magnitude is determined

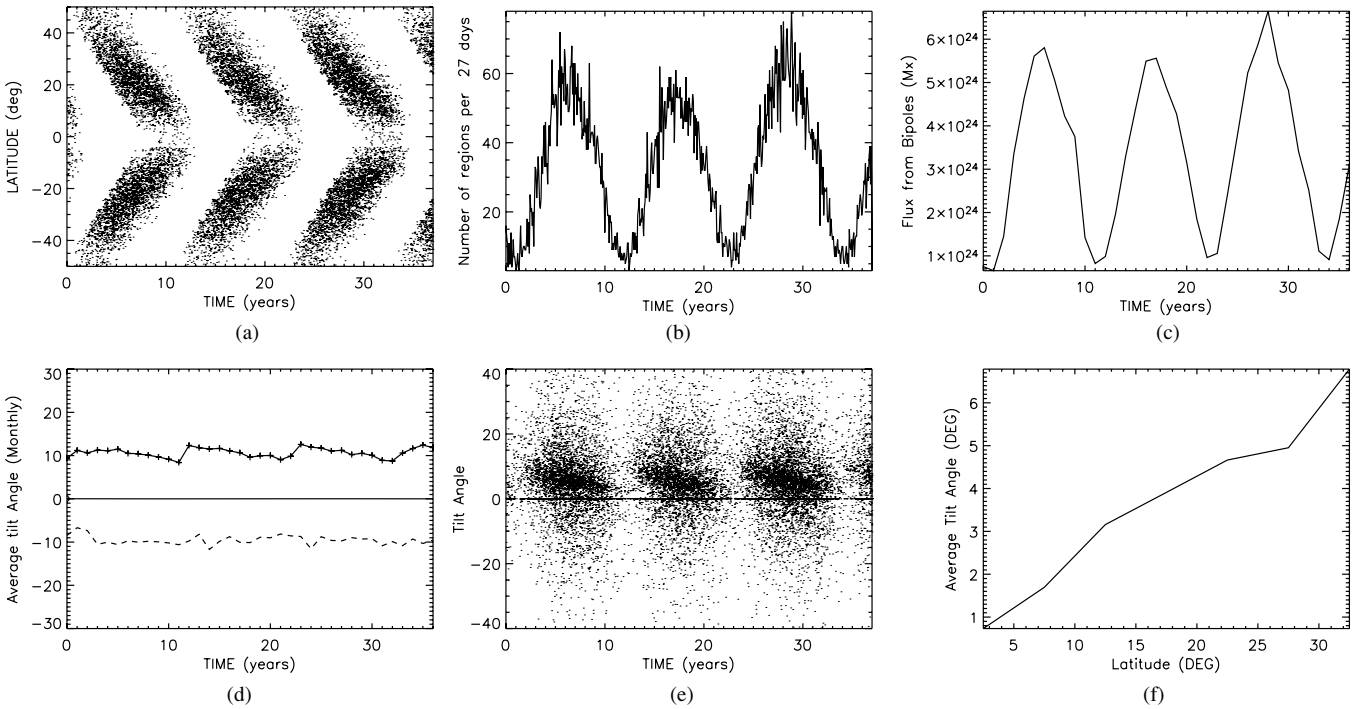

Figure 3. Graphs showing the properties of the bipoles emerged within the simulation. (a) The distribution of bipole emergences as a function of time and latitudes, (b) the numbers of bipoles emerging per 27 days, (c) the flux emerging within the bipoles per 27 days, (d) the average monthly tilt angle of the bipoles, (e) tilt angle distribution throughout the simulation, and (f) the average tilt angle vs. latitude. The first cycle depicted in the above plots was used as a "control" cycle to initiate the simulation. The work presented here will only analyze cycles two and three where flux values have been scaled to KP synoptic data.

by comparing midlatitude field strengths within the simulation with those determined from observations. In the simulations, the profile of $u(\theta)$, the meridional flow, given as a function of latitude ($\lambda = \pi/2 - \theta$) is

$$u(\lambda) = \begin{cases} -u_o \sin(\pi\lambda/\lambda_o), & |\lambda| < \lambda_o; \\ 0, & \text{otherwise}; \end{cases} \quad (2)$$

where above λ_o, the meridional flow velocity vanishes. For the simulations, we choose $\lambda_o = 75^\circ$ and $u_o = 11$ m s^{-1} as used by van Ballegooijen et al. (1998). For differential rotation, $\Omega(\theta)$, the profile of Snodgrass (1983) is used,

$$\Omega(\theta) = 13.38 - 2.30\cos^2\theta - 1.62\cos^4\theta - \Omega_o \quad (\text{deg day}^{-1}), \quad (3)$$

where Ω_o is the Carrington rotation rate (13.2 deg day^{-1}).

To evolve the radial field component forward, Equation (1) is expressed in terms of spherical harmonic functions where

$$B_r(r = R_\odot, \theta, \phi, t) = \sum_{l=1}^{N} \sum_{m=-l}^{l} B_{lm}(R_\odot, t) \times Q_{lm}(\theta) e^{im\phi}, \quad (4)$$

where $B_{lm}(R_\odot, t)$ represent the time-dependent complex fourier coefficients at the solar surface, $Q_{lm}(\theta) = P_{lm}(x = \cos\theta)$ are associated Legendre functions, l is the harmonic degree, m is the azimuthal mode number, and N is the number of harmonics. By substituting Equation (4) into Equation (1), it can be shown that the time variation of B_r through its fourier coefficients is

$$\frac{\partial B_{lm}}{\partial t} = \sum_{l'=|m|}^{N} (F_{u,l'lm} - imG_{\Omega,l'lm}) B_{l'm} - Dl(l+1)B_{lm}, \quad (5)$$

where

$$F_{u,l'lm} = 2\pi \int_0^\pi u(\theta) Q_{lm}(\theta) \frac{dQ_{l'm}}{d\theta} \sin\theta d\theta, \quad (6)$$

$$G_{\Omega,l'lm} = 2\pi \int_0^\pi \Omega(\theta) Q_{lm}(\theta) Q_{l'm}(\theta) \sin\theta d\theta \quad (7)$$

represent the effects of meridional flow and differential rotation on the spherical harmonics. These couple modes of different l but the same value of m. The final term in Equation (5) represents the effect of diffusion, where each of the modes diffuse independently of one another (higher order l modes diffuse faster).

The instant day simulations are run for three solar cycles. The first cycle is used to remove the unrealistic initial starting condition of a purely axisymmetric polar field, while the two later cycles are used to study the variation of coronal null points. The dipole strength at the start of the simulation is chosen such that in all the three cycles the polar fields reverse one to two years after cycle maximum. The first cycle is not considered any further in this study. The amount of flux emerging within the later two cycles is matched to that found in KP synoptic magnetograms for cycles 21 and 22 by approximately matching flux values over the whole solar surface and at 40° latitude. A latitude of 40° is chosen as no significant large-scale emergences are expected throughout the solar cycle above this latitude. Therefore, the polar fields and global dipole within the simulation is self-consistently produced by the flux passing through this latitude and subsequent surface diffusion. In each cycle, approximately 4000 bipoles are emerged. Figure 3 presents the statistical properties of the bipoles. Five bipole sizes are used ranging from 10^{19} Mx to 10^{22} Mx (Mackay et al. 2002; Mackay & Lockwood 2002). Combining these with the wide range of tilt angles, polarity separations and latitudes of

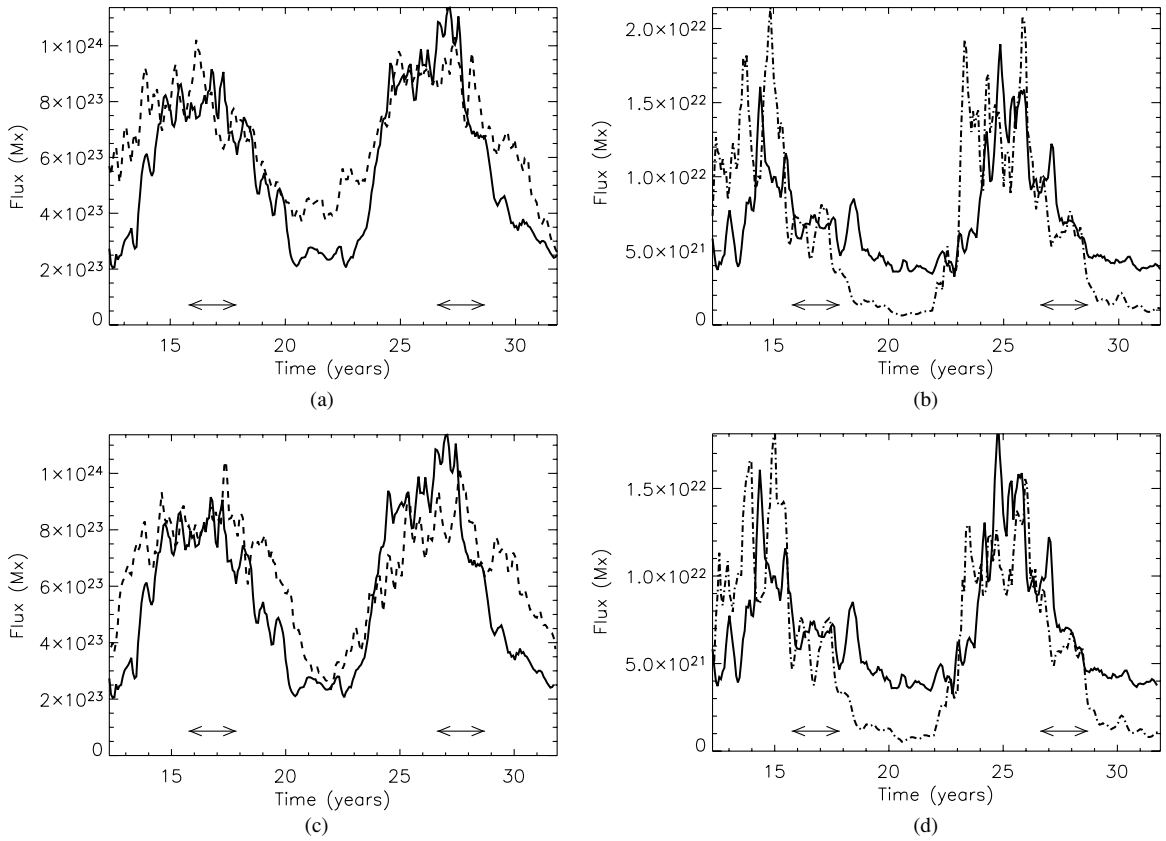

Figure 4. Graphs showing the surface flux from our "instant day" simulation ((a) and (b)) and the simulated synoptic magnetograms ((c) and (d)). Graphs (a) and (c) give the total surface flux while (b) and (d) give the flux at 40° latitude. In each case, the solid lines denote the flux values deduced from the Kitt Peak synoptic magnetograms where the dashed curve denotes the results of the simulations. The double-ended arrows in each graph denote a two year time period around cycle maximum determined from the peaks in bipole emergence rate.

emergence, significantly affects how the total flux on the solar surface evolves over time. The latitude distribution of emerging bipoles (Figure 3(a)) follows the classic butterfly diagram. The number of bipoles emerging (Figure 3(b)) follows a cyclic variation similar to that of the sunspot number. In agreement with this, the amount of flux emerging every 27 days also follows a cyclic pattern (Figure 3(c)). The average tilt angle of the bipoles (Joy's law, Figure 3(d)) decreases throughout the solar cycle, with the value at lower latitudes being less than that at higher latitudes. In Figure 3(e), the distribution of bipole tilt angles can be seen where there is a wide scatter in the data as found in observations, but where the majority of the bipole tilt angles satisfy Joy's law. Finally in Figure 3(f), the average bipole title angles can be seen as a function of latitude of emergence. Note that the tilt angle does not follow the $\lambda/2$ variation used in previous studies (Mackay et al. 2002; Mackay & Lockwood 2002) but has a much shallower variation such as that suggested by Schüssler & Baumann (2006).

In the instant day simulations by varying the bipole properties to those shown in Figure 3, the flux levels over the entire surface and at 40° latitude are matched with KP synoptic magnetograms (Figures 4(a) and (b)). The fluxes match fairly well over (a) the whole surface and at (b) 40° latitude. For (b) a similar graph was found for the southern hemisphere. The peaks in flux occur at approximately the same time, as do the minima. Slightly higher flux values are found within the "instant day" simulation. We attribute this to the fact that the instant day simulation generates the whole surface field and does not lose information—which occurs in the construction of KP synoptic magnetograms. As described earlier, the KP synoptic magnetograms lose data by missing some emerging active regions and therefore have a lower flux than what occurs in reality on the Sun. A better comparison between the observations and the simulations is to compare the observed data with "simulated synoptic data," as these data sets are constructed in a similar manner.

2.2.2. Simulated Synoptic Magnetogram Conversions

In order to convert the "instant day" maps into the form of simulated synoptic magnetograms, the relevant data from each of the instant day maps must be identified and extracted. To do this, initially a latitudinal strip with a width of 13°.5 longitude is taken from the rightmost edge of the first "instant day" map. This portion of the instant day map is defined to be the portion that is initially lying at central meridian. This information is then stored as the rightmost strip of the first simulated synoptic magnetogram. A second latitudinal strip, of the same width, is then taken from the left edge of the previous strip in the instant day map, representing the fact that this would be the next strip to lie at central meridian. This is then stored as the next section of the simulated synoptic magnetogram. This method is then continued over 27 days of the "instant day" maps, making up a single simulated synoptic magnetogram covering one Carrington rotation. This process is then repeated with each successive 27 day period of the instant day simulation, producing a subsequent simulated synoptic magnetogram. Once constructed, the simulated synoptic magnetograms are then corrected for flux balance which usually involves only a small correction.

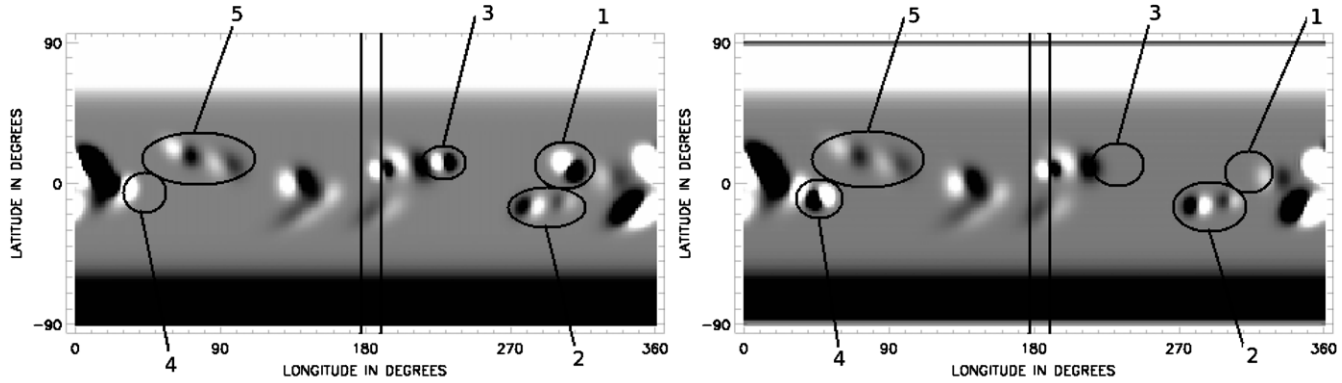

Figure 5. Image showing (a) a typical instant day map and (b) a simulated synoptic magnetogram covering the same 27 day rotation period. The area within the vertical black lines corresponds to the portion of the instant day map that lies at central meridian and is extracted and inserted into the simulated synoptic magnetogram. Several key features have been marked on both the "instant day" map and the simulated synoptic magnetogram.

A comparison of a single instant day map (Figure 5(a)) and a simulated synoptic map (Figure 5(b)) shows that the technique produces a good average representation of the field over a single rotation. To check that the conversion has correctly worked, we compare several features between the instant day and the simulated synoptic magnetograms. The black line in Figure 5(a) denotes the portion of the instant day map that lies at central meridian. This portion of the map is also highlighted in the simulated synoptic map. The information to the right of the black-lined section in Figure 5(b) has already been extracted from the instant day maps, while the information to the left has yet to be extracted in relation to the shown instantaneous map. Comparing feature 2 in both images shows that in the "instant day" map the active regions appear slightly weaker, and more longitudinally sheared than in the simulated synoptic magnetogram due to its extraction at an earlier time. Feature 5 shows bipolar regions, within the "instant day" map that have yet to be extracted for the simulated synoptic magnetogram. These bipolar regions appear less sheared and stronger than the corresponding regions in the simulated synoptic magnetogram. Therefore, this shows the opposite effect to that of feature 2, where the large-scale solar flows and diffusion have not had as much of an effect upon it, as they will have by the time the field information is extracted. Feature 4 shows a bipole that is yet to emerge in the "instant day" map, but is picked up for the simulated synoptic magnetogram. Conversely, features 1 and 3 show two bipolar regions that have been missed by the conversion into simulated synoptic magnetogram form. This is a key point, as information may be missed when converting into synoptic form thereby artificially impacting the complexity of the field distribution.

After converting the instant day maps into simulated synoptic magnetograms, the same flux measurements are taken as before, shown in Figure 4. The simulated synoptic magnetograms show a better match than the instant day maps. The peaks of flux at solar maximum occur at approximately the same time and magnitude. The minima give a better match between the two data sets than before. This is because the simulated synoptic magnetograms lose some information compared to the instant day simulations (in the same way that the KP magnetograms lose information). By comparing the simulated synoptic magnetograms to the KP synoptic magnetogram, data produced by a similar technique are compared. From this we have confirmation that our low latitude field distributions are realistic and subsequently will produce realistic high latitude fields.

2.2.3. Extrapolation of a Potential Field.

Once the flux levels in the simulations are matched with KP synoptic magnetogram levels, a coronal magnetic field must now be constructed. Within the solar corona the Lorentz force is the dominant force and any magnetic field that is in equilibrium satisfies to zeroth order the force-free field equation, $\mathbf{j} \times \mathbf{B} = 0$. As a result, the electric current, $\mathbf{j} = 1/\mu_o \nabla \times \mathbf{B}$, can be written as $\mathbf{j} = \alpha(\mathbf{r})\mathbf{B}$. The two most useful class of solution to the force-free field equation occur when $\alpha = 0$ (a potential magnetic field) and $\alpha = \alpha(\mathbf{r})$ (a nonlinear force field). When α is non-zero, the magnetic field may be regarded as being sheared. Observations of the solar corona in Hα and X-rays show localized, highly sheared regions called solar filaments and sigmoids, along with less or very weakly sheared regions such as coronal loops. Alternatively, white light coronagraphic observations show that the large-scale global field may be approximately represented by a field which is close to potential. In recent years, much work has been done in constructing global MHD models based from single extrapolations (Riley et al. 2006) or nonlinear force-free field evolutions over a period of months based on observed magnetograms (Yeates et al. 2007, 2008; Yeates & Mackay 2009). In the study of Riley et al. (2006), the authors found that global potential field solutions closely matched those found from MHD simulations, at large scales, when extrapolations are carried out; since our study mainly deals with the topology of the large-scale coronal structures, we believe that a potential field extrapolation of the coronal field is adequate for our purposes.

A potential field is extrapolated out to 2.5 solar radii for both the "instant day" and "simulated synoptic magnetograms" using the surface spherical harmonics $B_{lm}(R_\odot, t)$ for each case. The potential magnetic field is found by solving Laplace's equation with inner and outer boundary conditions given by $B_r(R_\odot, \theta, \phi, t)$ and $B_\theta = B_\phi = 0$ at $R_{ss} = 2.5\,R_\odot$, respectively. It may be easily shown that for fixed boundary conditions the potential magnetic field is both unique and the lowest energy solution. For a potential magnetic field,

$$\nabla \times \mathbf{B} = 0 \Rightarrow \mathbf{B} = -\nabla\Psi,$$

where Ψ is some unknown scalar function. Combining this with

the solenoidal constraint $\nabla \cdot \mathbf{B} = 0$, means that Ψ must satisfy

$$\nabla^2 \Psi = 0.$$

Solutions of Laplace's equation in spherical coordinates are well known (Jackson 1962),

$$\Psi(r, \theta, \phi) = \sum_{l} \sum_{m=-l}^{l} [a_{lm} r^{l} + b_{lm} r^{-(l+1)}] \times Q_{lm}(\theta) e^{im\phi},$$

where a_{lm} and b_{lm} are unknown and $Q_{lm}(\theta) = P_{lm}(x = \cos\theta)$. From this expression, the radial field becomes

$$B_r(r, \theta, \phi, t) = \sum_{l=1} \sum_{m=-l}^{l} B_{lm}(r, t) Q_{lm}(\theta) e^{im\phi},$$

where $B_{lm} = -l a_{lm} r^{l-1} + (l+1) b_{lm} r^{-l-2}$. Through determining similar equations for B_θ and B_ϕ, and applying the outer boundary conditions it may be shown that

$$\mathrm{B}_{lm}(\mathrm{r}, \mathrm{t}) = \mathrm{B}_{lm}(R_\odot, \mathrm{t}) \times \left[\frac{(l+1)\left(\frac{\mathrm{r}}{R_\odot}\right)^{-l-2} + l\left(\frac{\mathrm{R}_{ss}}{R_\odot}\right)^{-2l-1}\left(\frac{\mathrm{r}}{R_\odot}\right)^{l-1}}{l + 1 + l\left(\frac{\mathrm{R}_{ss}}{R_\odot}\right)^{-2l-1}} \right].$$

Therefore, the higher the model number, l, the faster the mode falls off with radial distance. Through knowing B_r, the B_θ and B_ϕ components may be uniquely determined using $\nabla \cdot \mathbf{B} = 0$ and $\mathbf{B} = -\nabla\Psi$ to first determine Ψ and then the horizontal field components where

$$B_\theta(r, \theta, \phi, t) = \sum_{l} \sum_{m=-l}^{l} C_{lm} \frac{\partial \mathrm{Q}_{lm}(\theta)}{\partial \theta} e^{im\phi},$$

$$\mathrm{B}_\phi(r, \theta, \phi, t) = \sum_{l} \sum_{m=-l}^{l} \frac{im}{\sin\theta} C_{lm} \mathrm{Q}_{lm}(\theta) e^{im\phi},$$

and

$$C_{lm}(r, t) = B_{lm}(R_\odot, t) \times \left[\frac{\left(\frac{r}{R_\odot}\right)^{-l-2} - \left(\frac{R_{ss}}{R_\odot}\right)^{-2l-1}\left(\frac{r}{R_\odot}\right)^{l-1}}{(l+1) + l\left(\frac{R_{ss}}{R_\odot}\right)^{-2l-1}} \right]$$

are the mode amplitudes associated with the angular components of the field. Note that the equations defining the three components of **B** contain both real and imaginary terms where only the real parts are considered physical and used within this study.

2.2.4. Null Point Finding Method

In order to scan the simulation for the location of coronal null points, the trilinear null finding method of Haynes & Parnell (2007) is used where it is adapted to work in spherical coordinates. The method is split into three distinct parts: reduction, trilinear analysis, and then locating the null point to sub-grid resolution through a root finding technique. In the reduction stage, every grid cell is scanned and a simple test is used to determine whether or not a null point may exist. A necessary but not sufficient condition for a null is that all the three field components as defined on the corners of the cube must reverse sign. Applying this condition reduces the number of cells from 1,212,416 to 20,718 in the "instant day" simulations (1.7% of the cells are retained) and to 15,833 in the simulated synoptic magnetograms (1.3% of the cells are retained).

The second stage of the method is a trilinear analysis of each cell that is remaining. This is based on the fact that if a null point exists then it must lie on all three of the zero curves, $\mathrm{B}_r = \mathrm{B}_\theta = 0$, $\mathrm{B}_\theta = \mathrm{B}_\phi = 0$, and $\mathrm{B}_\phi = \mathrm{B}_r = 0$. The existence of such curves is first considered on the faces of each cell, where the lines $\mathrm{B}_r = 0$, $\mathrm{B}_\theta = 0$, and $\mathrm{B}_\phi = 0$ are considered. To consider this, each field component is expressed in terms of a bilinear equation,

$$\mathrm{B}_i = a_i + b_i x + c_i y + d_i x y, \tag{8}$$

where i indicates the component of the magnetic field considered, and x and y represent the spherical coordinates within the plane of the cell face. For simplicity, it is assumed that the range of each x and y value is normalized such that $0 \leqslant x \leqslant 1$ and $0 \leqslant y \leqslant 1$. The constants are determined from the values of the field on the cell corners such that $a_i = \mathrm{B}_{i(0,0)}$, $b_i = \mathrm{B}_{i(1,0)} - \mathrm{B}_{i(0,0)}$, $c_i = \mathrm{B}_{i(0,1)} - \mathrm{B}_{i(0,0)}$, and $d_i = \mathrm{B}_{i(1,1)} - \mathrm{B}_{i(1,0)} - \mathrm{B}_{i(0,1)} - \mathrm{B}_{i(0,0)}$ (where $\mathrm{B}_{i(0,0)} = \mathrm{B}_i(0, 0)$). To solve for any single intersection, pairs of equations $\mathrm{B}_i = \mathrm{B}_j = 0$ are considered and the values of x and y which satisfy this and lie between $0 \leqslant x \leqslant 1$ and $0 \leqslant y \leqslant 1$ are found.

These points represent the location where zero curves threading through the interior of the cell cross the boundary of the cell. A necessary condition for a single null to occur in the cell is that each possible combination of these zero curves, must pierce the boundary of the cell in pairs, however, it is possible for one zero curve to cross the boundary at more than one pair of points. A null exists along any given zero curve if and only if the third component of the field is of opposite sign at the endpoints which lie on the face.

Once the existence of a null has been confirmed, it is then located down to sub-grid resolution using a three-dimensional version of the Newton–Raphson method for finding roots of equations. The Newton–Raphson method is repeated until $|\mathbf{B}| \leqslant 1e-4$. Various starting points are used until the iterative method is successful within the cell. Should the method fail, the grid is then split up into eight sub-grid cells, using trilinear interpolation, and the trilinear process is then repeated on these sub-cells.

While the trilinear method will yield the location of nulls throughout the simulation. One key point is whether or not the null points are connected to the global dipole. This is key as it is only these that are affected by the reversal of the overlying global dipole on the Sun at solar maximum. Figure 6 shows two scans from the instant day simulation. In each case, the nulls have been located (crosses), and field lines plotted around them. The image on the top shows a null that has a connection with the global dipole, as the field lines around the null extend up into the polar regions. In the image on the bottom, several nulls are found and the field lines surrounding a typical example are plotted. This null has no connection with the overlying dipolar field on the Sun.

3. NULL POINT BEHAVIOR

The properties of the null points found within the global simulations are now considered where first the general properties of the null points throughout the simulations are discussed

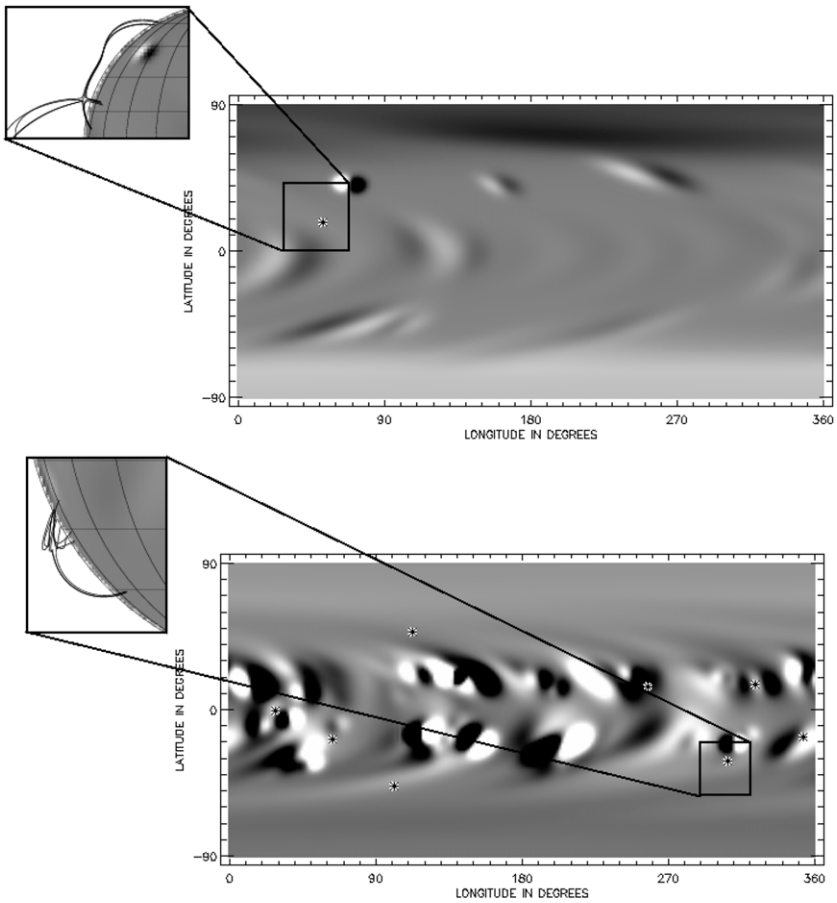

Figure 6. Images showing a field line plot around a null that is connected with the global dipole (top) and a set of nulls not connected with the global dipole (bottom).

(Section 3.1), next the number of nulls as a function of bipoles emergence rates is considered (Section 3.2), and finally the relationship between the nulls and their underlying photospheric flux distributions is shown (Section 3.3).

3.1. Null Point Variation

Figure 7 presents the variation of null points for both the instant day (a) and (b)) and simulated synoptic magnetogram cases (c) and (d) for cycles 2 and 3 which are simulated to match KP synoptic magnetograms. In each case, (a) and (c) show the variation in total number of null points per day as a function of time, and (b) and (d) show the number of null points connected with the overlying global dipole. The sampling rate is every 27 days. Both sets of graphs show that the number of null points varies cyclically with the emergence rate during the solar cycle. At solar minimum, there are fewer null points than at solar maximum. One of the main features of these graphs is that the number of coronal null points found is high with peak values at cycle maximum of 15–17 per day in the instant day simulation. It is clear that fewer null points are found in the simulated synoptic magnetograms. The total number of null points within either simulation is approximately one quarter to a third of the number of emerged bipoles (a total of 2843 in the "instant day" simulation and 2437 in the simulated synoptic magnetograms). Therefore, the simulated synoptic magnetograms lose approximately 1/6 of the total number of nulls (relative to the instant day simulations). This is due to the loss of information and complexity of the photospheric field encountered when creating the simulated synoptic magnetograms. This is an important caveat which must be kept in mind when using synoptic magnetograms to represent the actual field of the Sun. The number of null points connected with the global dipole is found to be a very small fraction of the total nulls. In the "instant day" maps, only 8% of the total null points are connected to the global dipole and in the simulated synoptic magnetograms it is only 7%. A key feature of both the graphs is that after solar maximum of each cycle there are no null points connected with the global dipole until the new solar cycle begins, as predicted in the schematic of Figure 1. However, as there are a similar number of nulls in both the rising and the declining phase, the creation of the majority of null points depends upon the configuration of the underlying active latitude flux and not on the global dipole. This implies that the magnetic breakout configuration as a model of CME initiation is not solar cycle phase dependent but is applicable, and indeed occurs, throughout the rising and declining phases.

Figure 8 shows the variation of null point properties within the "instant day" simulation for cycles 2 and 3 which are matched to KP. A similar graph is found for the simulated synoptic magnetograms; however, it is not shown here as its features are nearly identical to those shown in Figure 8. Figure 8(a) shows the distribution of null points with latitude. It can be seen that the majority of nulls are confined to $\pm 50^{\circ}$ latitude and therefore connect to the underlying active latitude flux. A key feature of these graphs is the presence of a significant number of null points over the equatorial region of the Sun. If null points occur in the equatorial plane, then the breakout model could possibly account for earthwardly directed CMEs in the equatorial plane. Figure 8(b) shows the average absolute value of latitude of null points over time. It can clearly be seen that as the solar cycle

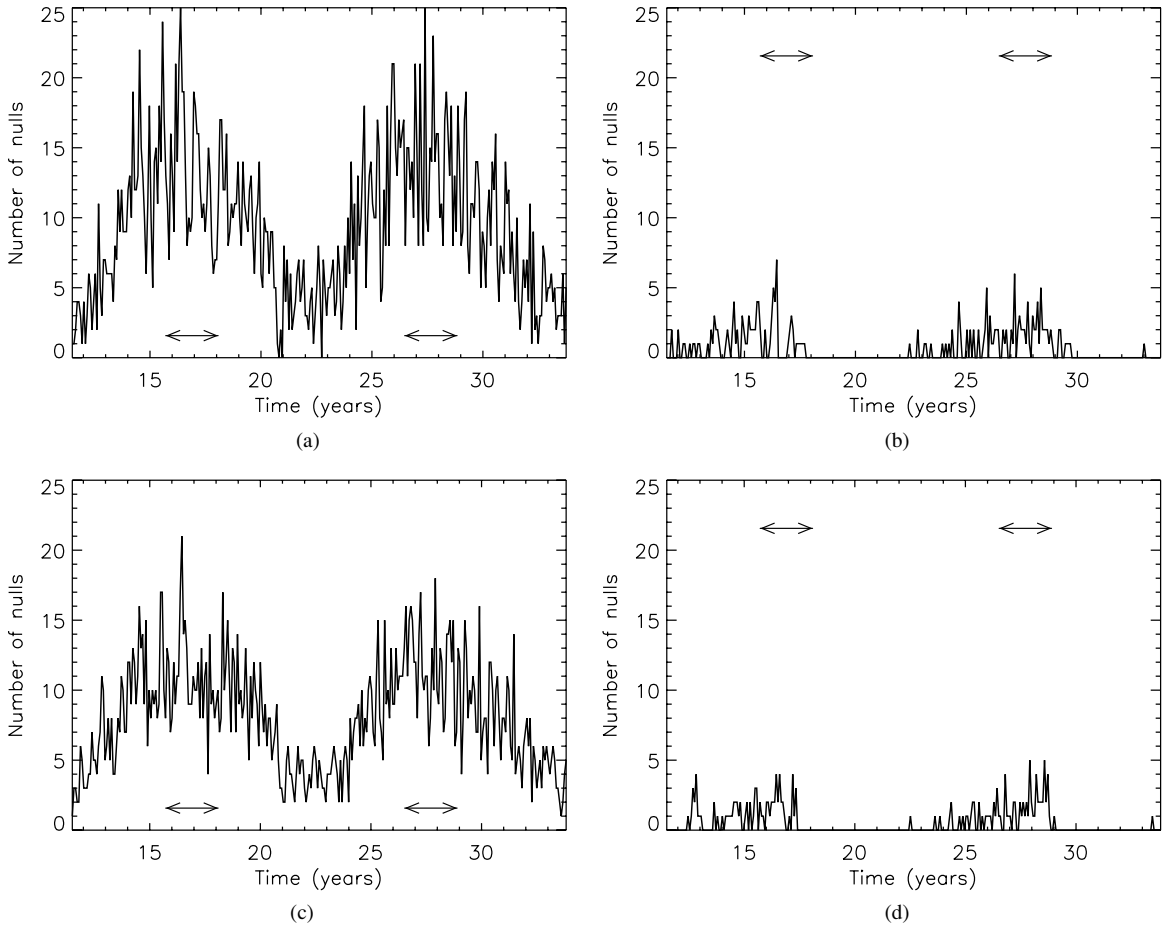

Figure 7. Graphs showing the variation in total number of nulls found in (a) the instant day simulation and (c) the simulated synoptic simulation. The number of those nulls connected with the overlying global dipole can also be seen for (b) the instant day map simulation and (d) the simulated synoptic simulation. The double-ended arrows in each graph denote a two year time period around cycle maximum determined from the peaks in bipole emergence rate.

progresses the null points occur at lower and lower latitudes following the butterfly diagram.

Figure 8(c) shows the average radial distance of the null points as a function of latitude. The average radial distance slightly increases as the null points occur closer to the equator; while it is true, the average radial distance remains very low in the corona (peaking below 1.25 solar radii). Figure 8(d) shows the number of coronal nulls against radial distance in the corona. From this graph, it can be seen that the majority of null points occur below 1.5 solar radii. For comparison, the dashed line denotes a line of slope -3 which indicates that the nulls fall off with radial distance as $1/r^3$. This matches the results of Longcope et al. (2003) who found this relation in terms of isolated point sources. Figure 8(e) shows the average radial distance of null points with time, and it can be seen that the coronal null radial distances follow a cyclic variation throughout the solar cycle. As the overlying global dipole weakens and the underlying field becomes stronger, the nulls reach higher into the corona. As the overlying dipole field strengthens in the declining phase of the cycle and the flux in the active region belt reduces, the nulls become restricted to lower radii. In the graphs described above a wide range of scatter is found. To consider whether averaging may reduce this and produce simpler trends, the present simulation has been extended by adding three additional theoretical cycles. Doing so only slightly reduces the scatter, so we believe that this scatter is a true feature where it is the result of the complicated underlying photospheric fields.

In Figure 9, butterfly distributions of the latitude of the null points are shown. The left-hand image shows the distribution of null point latitudes in the "instant day" simulation, the right-hand image shows the latitude distribution of null points in the "simulated synoptic magnetogram" simulation. It can be seen that the location of null points generally follows the pattern of sunspot emergence, with null points forming closer to the equator as the solar cycle progresses through the rising and declining phases. On comparing Figure 9 with Figure 3(a), it can be seen that the null point butterfly diagram has a much wider spread compared to the bipole emergence butterfly diagram. A noticeable feature is that there is a steady stream of null points forming closer to the polar caps around cycle maximum. After solar maximum and subsequent polar field reversal, these null points disappear until the following solar cycle begins. These are null points that are all connected with the overlying global dipole.

An important result from this study is that the majority of null points are dependent on the underlying active region flux. This means that the overlying global dipole reversal that occurs after solar maximum will not indicate a disappearance of null points throughout the declining phase of the solar cycle. While it is true that some nulls are linked to the global dipole, their numbers are not significant enough to indicate any decrease in applicability of the magnetic breakout model. The consequence of this is that null points will occur throughout the entire solar cycle, and the breakout model is applicable throughout all stages as a possible mechanism for CME initiation.

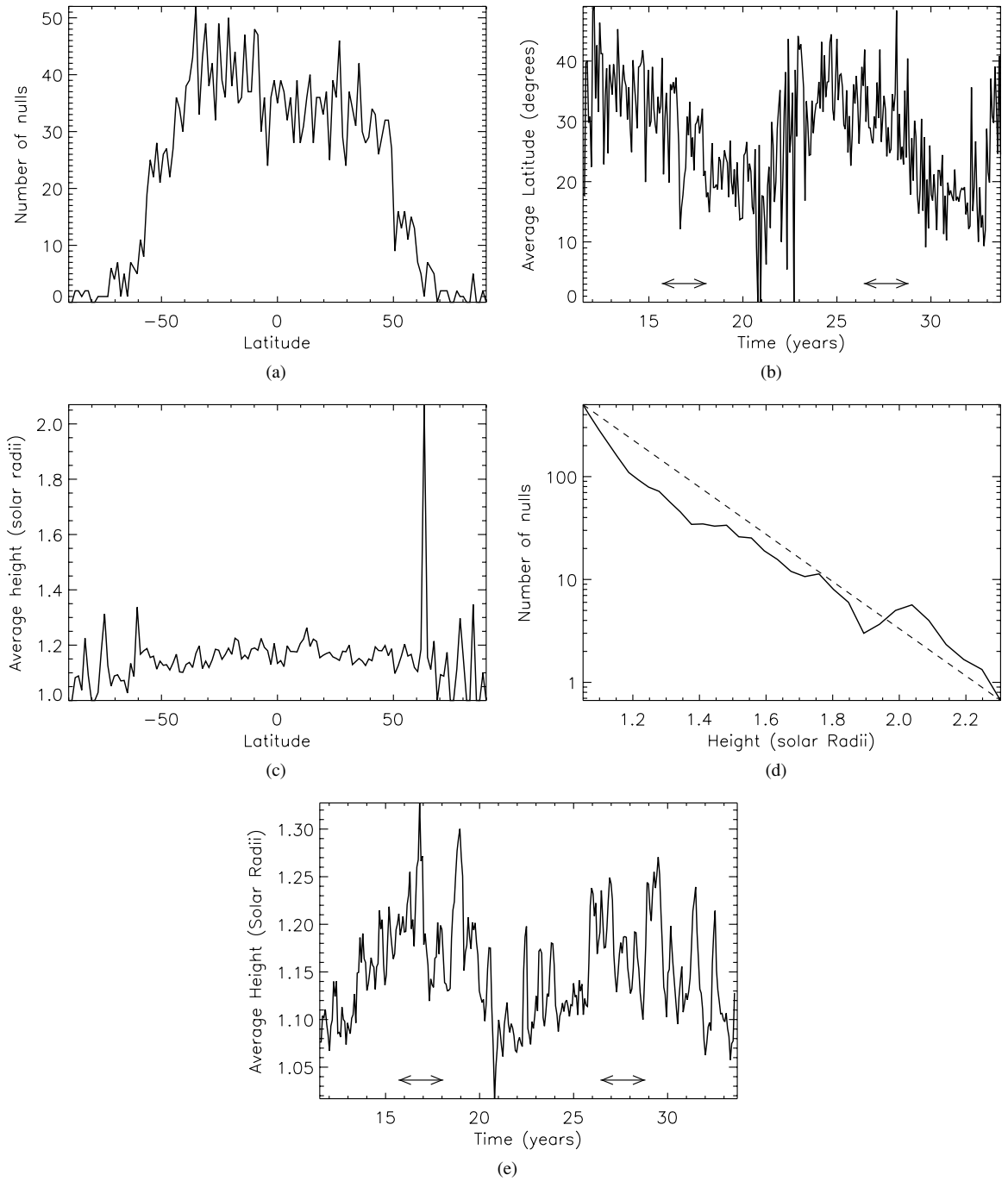

Figure 8. Graphs from the instant day map simulation showing (a) the distribution of nulls with latitude, (b) the average absolute value of latitude with time, (c) the average radial extent of a null with latitude, (d) the distribution of nulls with radial distance where the dashed straight line shows a gradient of −3, and (e) the average radial extent of a null with time. In (b) and (e), the double-ended arrows denote a two year time period around cycle maximum as determined from the peak in bipole emergence rate.

3.2. Null Point Numbers in Relation to Bipolar Emergence Rates

To understand how coronal null points depend upon the lower latitude active region flux, the relationship between the number of coronal null points and the emergence rates of the bipolar active regions is investigated. Figure 10 shows a scatter diagram of the number of coronal null points every 27 days against the number of bipolar regions emerged in that same 27 day period. It can be seen that there is a positive, linear association where there is roughly a relation of 1/3 of the bipoles emerged to the number of null points (denoted by the solid straight line; a best fit gives a gradient of 0.29). Even though there is a rough relation of a linear fit, it can be seen that there is a very wide scatter both above and below the line. This generally means that, as the number of bipoles emerged increases, so does the number of coronal null points present within the simulation. The number is less than the theoretical value of 1/2 (dashed line), assuming that a single null point can exist between every two bipoles that emerge in a quadrupolar configuration. However, the value of 1/2 still lies within the width of the scatter in the diagram. Therefore, active periods of solar cycles should have many more

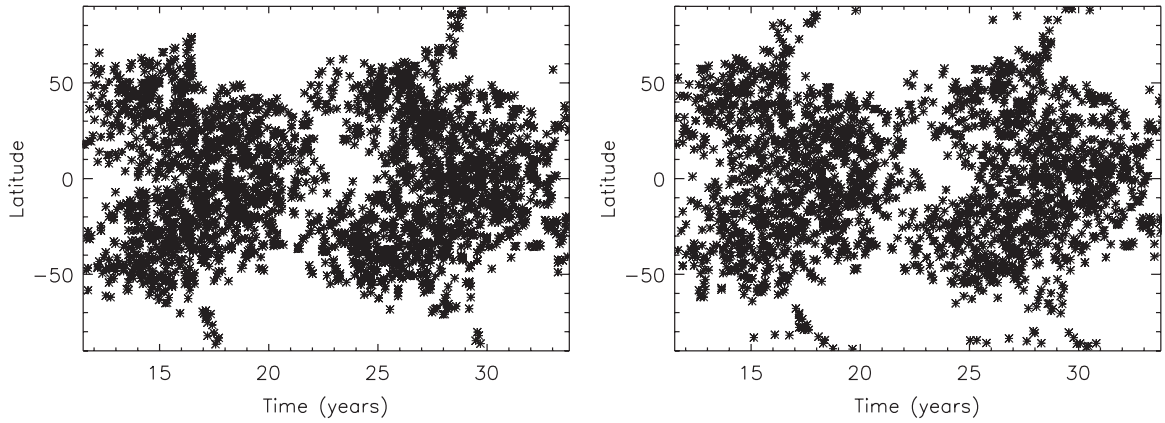

Figure 9. Butterfly diagrams showing the distribution of null points in (a) the "instant day" map simulation (left) and (b) the simulated synoptic magnetogram simulation (right).

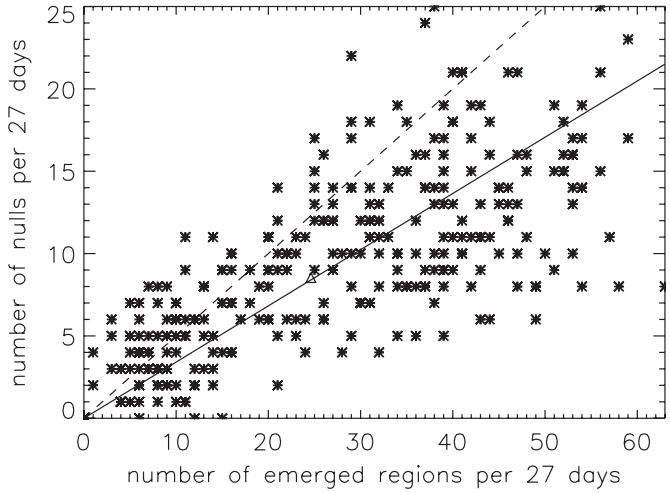

Figure 10. Scatter plot of the number of null points found every 27 days vs. the number of bipolar regions emerged every 27 days. The triangle in the center indicates the mean point of both data sets. The solid line denotes a gradient of 1/3 while the dashed line 1/2.

coronal null points than inactive periods and consequently more possible locations would exist for breakout configurations. An interesting feature can be seen in Figure 10 when the emergence rate of bipoles is low. When the emergence rate falls below 15 regions per 27 days an extremely wide scatter is found and there is no clear relationship between regions emerged and number of null points. The upper limit in the scatter provides a near one-to-one relationship between bipoles emerged and coronal nulls. The reason for this is discussed in Section 3.3, where the null points are classified relative to the underlying magnetic flux.

Figure 11 shows the number of coronal null points found in the "instant day" simulation when (a) 100%, (b) 75%, (c) 50%, and (d) only 25% of the bipoles were emerged. The number of bipoles is reduced by randomly removing them from the previous run. It can clearly be seen that, as the number of bipoles emerged within the simulation decreases, the total number of null points decreases. Between Figures 11(a) and (d), where the number of bipoles is reduced by 75%, we find that the total number of nulls reduces by 63%. Therefore, the loss in number of nulls is slightly less than that of bipoles, but the rates of decrease are consistent with one another and Figure 10. Therefore, the gradient of 1/3 obtained in Figure 10 only holds for large emergence rates and as the emergence rate dips to lower values, the results are not robust. The reason for this is explained in the next section where the location of null points is considered in relation to the distribution of radial flux at the photosphere.

3.3. Null Point Topology Classification

After locating all of the null points within the "instant day" simulation, the photospheric distribution that causes the coronal null point to exist is studied in order to classify them. The four types of photospheric distribution can be seen in Figure 12 and are defined as, from left to right, (a) the triple polarity configuration, (b) a newly emerged quadrupolar flux distribution, (c) an enclosed quadrupolar flux distribution which will occur across the equator as bipoles with opposite orientation in each hemisphere interact, and (d) an advected quadrupolar flux distribution. In each case, the star denotes the location of the coronal null. For each case, the top panel gives an idealized photospheric setup, while the bottom image is taken from the "instant day" map simulation and shows an actual example of each of the four photospheric flux distributions. On close inspection, it can be seen that cases (b) and (d) are the same from a topological standpoint. The distinction we are making between them is that (b) is formed by the emergence of bipoles in close proximity, while (d) requires convergence and interaction between the bipoles before a null can form. This information will enable us to determine whether configurations (a) or (d) are responsible for the extended width of the null point butterfly diagram.

Figure 13 shows the number and variation of null points that exist, within each of the four configuration types. It can be seen that the majority of coronal null points occur due to a newly emerged quadrupolar flux system on the photosphere (Figure 13(b)). The numbers of coronal nulls of this type of configuration vary cyclically with emerging bipole numbers, indicating their dependence upon the newly emerging bipoles within the solar cycle. Figure 13(d) shows the number of coronal nulls that are classified as an advected quadrupolar flux distribution on the solar surface. The number of nulls of this form starts off low at the start of the cycle. Then as the newly emerging surface flux begins to evolve due to meridional flow, differential rotation and diffusion, and bipoles converge toward one another. This causes the advected quadrupolar formations and associated null points to form. Figure 13(a) shows the number of coronal null points that are classified as a triple polarity photospheric configuration. These type of null points

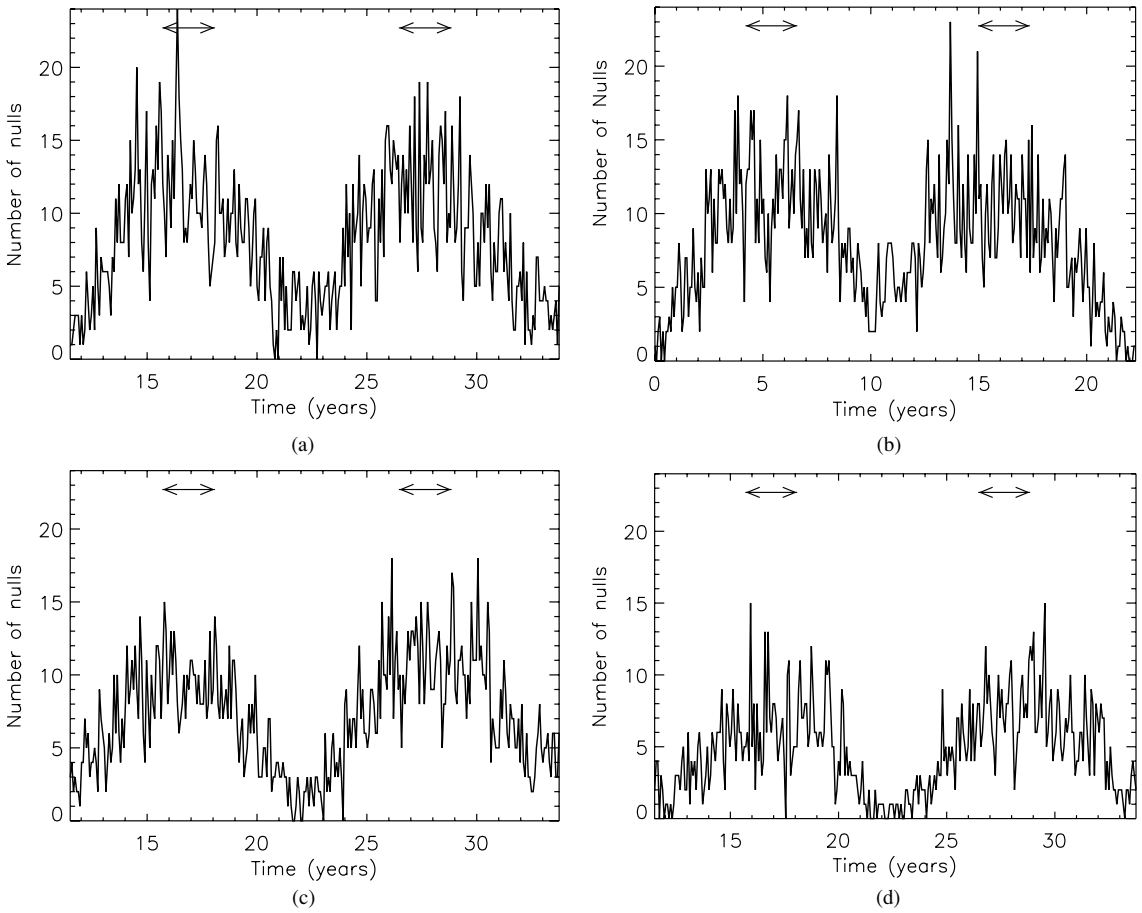

Figure 11. Graphs showing (a) the number of nulls found in the instant day map simulation with 100% of the bipoles emerged, (b) the number of nulls found in the instant day map simulation with 75% of the bipoles emerged, (c) the number of nulls found in the instant day map simulation with 50% of the bipoles emerged, and (d) the number of nulls found in the instant day map simulation with 25% of the bipoles emerged. The double-ended arrows in each graph denote a two year time period around cycle maximum determined from the peaks in bipole emergence rate.

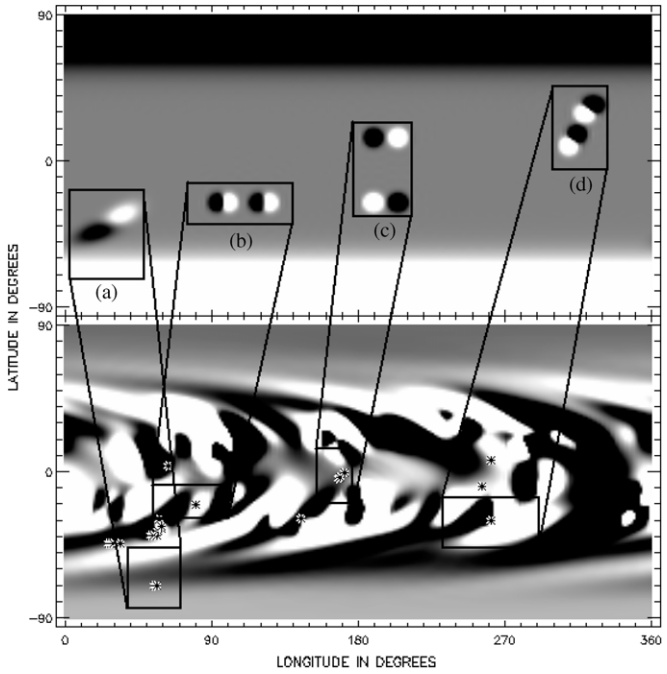

Figure 12. Image showing examples of the photospheric flux distributions used in order to classify the null point configuration. The first example is (a) a triple polarity configuration, (b) a newly emerged quadrupolar flux distribution, (c) an enclosed quadrupolar flux distribution, and (d) an advected quadrupolar flux distribution.

seem to occur throughout the rising phase of the cycle, and for a limited time after solar maximum, at which point they do not exist until the following cycle. This is due to the fact that the null points with this classification occur almost exclusively as pictured in Figure 12. The null is formed due to the magnetic field from one bipolar region and the polar field. At the start of the cycle and throughout the rising phase, the bipoles emerge at higher latitudes on the solar surface and in fewer numbers. This will cause several of the bipoles to have connections with the polar field within that hemisphere resulting in coronal null points. This clearly explains the wide scatter and tendency for higher number of nulls relative to emerged bipoles in Figure 10, when the number of emerging nulls are low. Later in the cycle, at approximately solar maximum and throughout the declining phase of the cycle, the bipolar regions emerge at lower latitudes and in greater numbers. This means that there are more interactions between the fluxes of one bipolar region and another, and nulls of a quadrupolar configuration are more likely to occur. This also explains why a 75% decrease in bipole emergence rates only results in a 68% decrease in the number of nulls. When fewer bipoles emerge there is an increased chance of a single bipole interacting with the polar field and producing a null, thus compensating for the decrease based on bipole–bipole interactions. As both the advected quadrupolar and triple polarity configurations have significant numbers, this illustrates why the width of the null point butterfly diagram is much wider than that of the bipole emergence butterfly diagram.

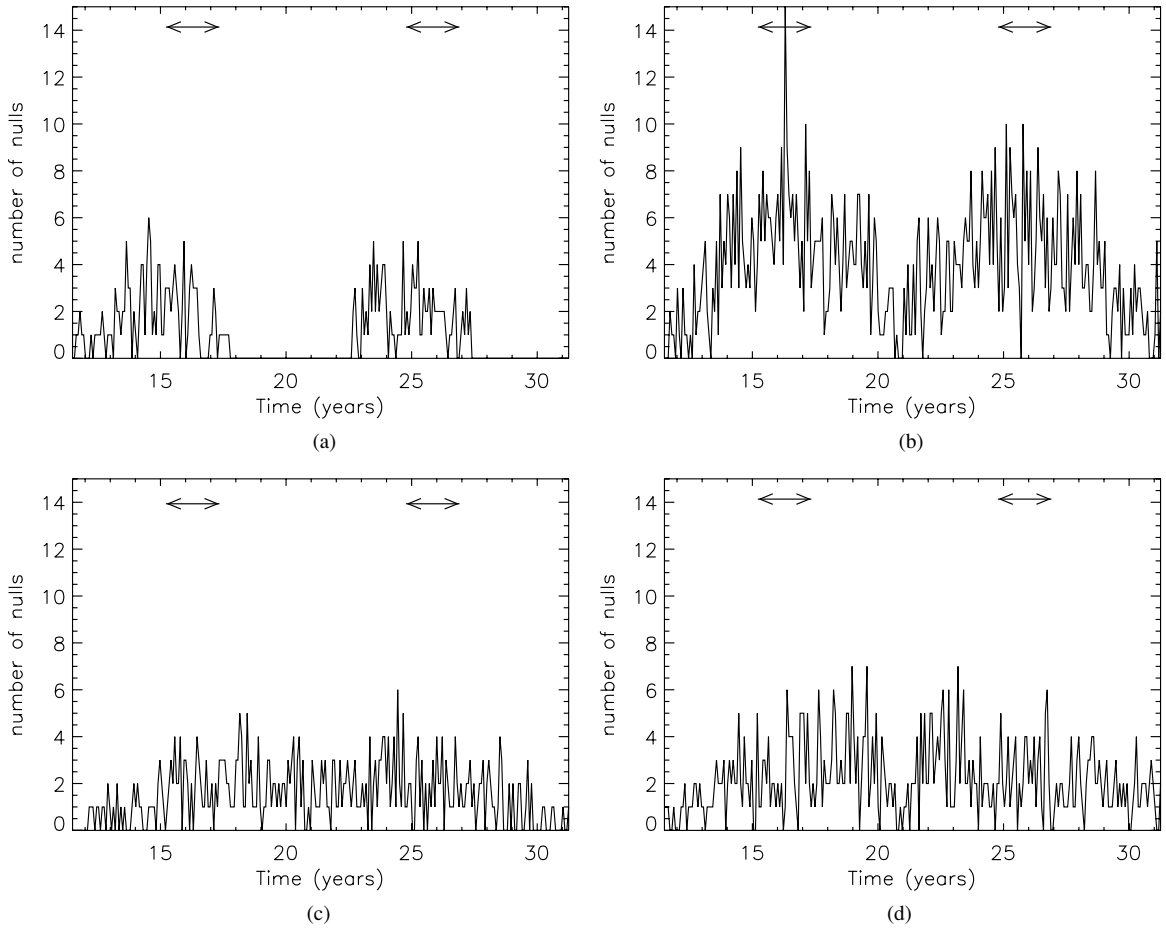

Figure 13. Graphs showing the classification of the null points within the "instant day" simulation. The graphs show results for (a) a triple polarity configuration, (b) a newly emerged quadrupolar configuration, (c) an enclosed quadrupolar configuration, and (d) an advected quadrupolar configuration. The double-ended arrows in each graph denote a two year time period around cycle maximum determined from the peaks in bipole emergence rate.

Null may form at any point, as bipoles are advected across the solar surface and not just when bipoles emerge. Figure 13(c) shows the number of coronal null points that are classified by an enclosed quadrupolar flux configuration on the photosphere. The number of null points of this type remains fairly constant throughout the simulation. A slight peak exists around solar maximum, due to the complexity of the photospheric field at that point, which has the highest rate of emergence. The constancy of this value fits the fact that these null points require cross-equatorial interactions and as bipoles emerge throughout the cycle at random longitudes there should be equal probability of this occurring.

In terms of all of the coronal null points that occurred in the simulation, approximately 45.3% had a photospheric flux distribution of the newly emerged quadrupolar type, 25.4% had an advected quadrupolar flux distribution on the photosphere, 17.6% had an enclosed quadrupolar photospheric flux distribution, and 11.7% have a triple polarity photospheric flux distribution. The triple polarity photospheric flux distributions are of a higher percentage compared to the number of nulls connected to the global dipole. This is because, in some cases, the triple polarity configurations may occur when bipoles interact with unipolar regions that do not lie at the poles.

4. CONCLUSIONS

In this paper, the existence of coronal null points has been considered through simulations of the Sun's global magnetic field. As coronal null points are a necessary element of the magnetic breakout model, it is expected that the location and variation of such null points will indicate possible CME source-region locations and their variation. As discussed in Section 1 and illustrated in Figure 1, the reversal of the global dipole in the declining phase of the solar cycle may have significant consequences for the existence of coronal null points and therefore on the issue of the solar cycle phase dependence of the breakout model. The reversal of the global dipolar field and the orientation (tilt-angle) distribution of solar active regions are intimately related in the context of the solar dynamo mechanism (Nandy & Choudhuri 2001; Yeates et al. 2008), and therefore connects magnetic field dynamics in the solar interior to coronal activity.

To model the variation of the Sun's global magnetic field, both at the level of the photosphere and corona, a combination of magnetic flux transport and PFSS models are applied. The locations and properties of the coronal null points are then considered through two distinct, but related, data sets prescribing the lower photospheric boundary condition. The first data set which we call the "instant day simulation" considers the flux distribution produced by the flux transport simulation and may be regarded as a true representation of the whole Sun magnetic field. This prescribes the radial field over the whole solar surface at any instant in time. The second data set, which we call the "simulated synoptic" data set considers the existence of coronal null points when the instant day simulation is used to produce synoptic magnetograms in a manner similar to that

carried out by KP (i.e., when limited observations are present and we can only view a portion of the solar disk). Through considering both data types, we were able to categorize what effect such a synoptic approximation makes on the number and location of coronal null points. Although this study is carried out with theoretical simulations, the flux values of these simulations are constrained by observations from KP. The present study differs from that of previous studies (Barnes 2007) as it considers the large-scale global field, rather than small-scale isolated regions.

Both the instant day and simulated synoptic simulations show that the number of coronal nulls varies cyclically throughout the simulation and in phase with the emergence rate of new flux. As the emerging flux follows the well-known butterfly diagram, the location of coronal nulls follows a similar pattern. There is however a difference in the structure of the butterfly diagram for the nulls as it shows a polar drift in the rising phase of the solar cycle. Over the two simulated cycles considered, a total of 2843 coronal nulls were found for the instant day simulations and 2437 for the simulated synoptic magnetograms. Therefore, through the process of forming synoptic magnetograms approximately 1/6 of the nulls are lost. This is a significant but acceptable number. At cycle maximum for the instant day simulations, the number of null points peaks at around 15–17 per day. When the number of nulls are compared to the rate of bipole emergence, a wide scatter is observed; however, on average, the ratio of nulls to emerged bipoles is approximately 1/3. Active cycles should therefore have many more coronal null points and breakout configurations than inactive ones. As the properties of the null points in the simulated synoptic magnetograms give similar results to that of the instant day simulations, only results from the latter simulations are discussed from now on.

On studying the latitudes of formation of the nulls, it is found that the vast majority of nulls form within the active latitude belts of $\pm 50^{\circ}$, with only very few forming outside this range. This indicates that it is the complex underlying active regions fields that are key in forming the coronal nulls and not the interaction of single bipoles with the global dipole. This is supported by the result that only 8% of the total number of nulls found were connected to the global dipole. As the vast majority of nulls are not connected to the global dipole, there is no significant change in the number of nulls between the rising and declining phases; therefore, the breakout configurations occur throughout the solar cycle. The hypothesis presented in Section 1 and Figure 1 is found to be true for nulls connected to the global dipole, however, their numbers are not significant.

As the majority of the coronal nulls are found to form at active latitudes, due to the complex structure of the underlying photospheric fields, a consequence of this is that the nulls form low down in the corona. An average radial extent of 1.25 $R_{\odot}$ (175,000 km above the photosphere) is found. In addition, the number of nulls falls off as $1/r^3$, as predicted by Longcope et al. (2003). When the null points are classified depending upon the photospheric flux distribution leading to their creation, it is found that 71% form in quadrupolar flux distributions (either newly emerged quadrupoles—46%, or advected quadrupoles—25%), 18% form around the equator due to cross-hemisphere bipole interactions, while only 11% are due to the interaction of single bipoles with unipolar regions of flux such as the polar fields.

In previous studies such as that of Barnes (2007), the authors have considered a direct one-to-one comparison of coronal nulls and CMEs as a test for the magnetic breakout model based on extrapolations from magnetograms with limited field of view. Such a one-to-one comparison would not be useful in the present study as we are not considering actually observed configurations, but rather simulated configurations based on global coronal modeling. Therefore, we restrict ourselves to comparing the qualitative behavior uncovered in our simulations to observations.

Over the years, much work has been done to calculate the variation of CMEs throughout the solar cycle (Cremades & St. Cyr 2007). Using all of the coronagraph data collected so far, almost three solar cycles worth, Cremades & St. Cyr (2007) found that CMEs follow a cyclic variation throughout the solar cycle, with more occurring at solar maximum and fewer at solar minimum. This fits the general variation of coronal null points found in this paper. Moreover, detailed analysis of the properties of CMEs and their source-region variation over the solar cycle indicate that, in fact, the spatio-temporal distribution of CME sources do follow the sunspot butterfly diagram rather closely (Yashiro et al. 2004; Cremades et al. 2006; Howard et al. 2008). A comparison with Figure 2 of the latter two works (where the observed CME time–latitude butterfly diagrams are plotted) shows that our simulated variation of coronal null points (Figure 9) agrees remarkably well with the observations. The reason is that the coronal null point distribution (or breakout topology) is simply coupled to active region distribution; its dependence on the phase (i.e., rising or declining) of the solar cycle and to the global dipolar orientation is minimal, as uncovered through our simulations.

In summary, we have considered the properties and variation of coronal null points in full Sun global simulations over two solar cycles. These null points are a key ingredient of the magnetic breakout model first proposed by Antiochos (1998) as a model for the initiation of CME's. The results of this study show that the majority of null points (over 90%) do not connect to the global dipole, and therefore there is no significant variation in the abundance of breakout configuration between the rising and declining phases of the solar cycle (other than that related to just asymmetry in sunspot numbers). The lack of dependence of the majority of the null points upon the global dipole is one of our key conclusions. As a consequence, in principle, the magnetic breakout model remains equally applicable at all stages of the solar cycle as an initiation mechanism for CMEs.

The authors thank STFC for their funding and Kitt Peak for the synoptic magnetogram data used in this project. NSO/Kitt Peak data used here are produced cooperatively by NSF/NOAO, NASA/GSFC, and NOAA/SEL. D.H.M. thanks UK STFC for financial support, the Royal Society for funding a 81 processor supercomputer under their Research Grants Scheme and the British Council for their financial support through the Research Exchange Program. D.N. acknowledges financial support from NASA through grant NNX07AT19G and from the Department of Science and Technology, Government of India through the Ramanujan Fellowship. The authors thank Colin Beveridge, Eric Priest, and Rhona Maclean for their helpful discussions, and the referee for his detailed report which has enhanced this paper.

REFERENCES

Antiochos, S. K. 1998, ApJ, 502, L181
Antiochos, S. K., DeVore, C. R., & Klimchuk, J. A. 1999, ApJ, 510, 485
Archontis, V., Moreno-Insertis, F., Galsgaard, K., Hood, A., & O'Shea, E. 2004, A&A, 426, 1047

Aulanier, G., Pariat, E., & Démoulin, P. 2005, A&A, 444, 961
Barnes, G. 2007, ApJ, 670, L53
Baumann, I., Schmitt, D., & Schüssler, M. 2006, A&A, 446, 307
Beveridge, C., Priest, E. R., & Brown, D. S. 2002, Sol. Phys., 209, 333
Beveridge, C., Priest, E. R., & Brown, D. S. 2004, Geophys. Astrophys. Fluid Dyn., 98, 429
Brown, D. S., & Priest, E. R. 1999, Proc. R. Soc. Ser. A, 455, 3931
Brown, D. S., & Priest, E. R. 2001, A&A, 367, 339
Chen, J. 1989, ApJ, 338, 453
Chen, J. 1996, J. Geophys. Res., 101, 27499
Choe, G. S., Cheng, C. Z., Lee, J., Lynch, B. J., Antiochos, S. K., Devore, C. R., & Zurbuchen, T. H. 2005, AGU Spring Meeting Abstracts, 2
Cremades, H., Bothmer, V., & Tripathi, D. 2006, Adv. Space Res., 38, 461
Cremades, H., & St. Cyr, O. C. 2007, Adv. Space Res., 40, 1042
Démoulin, P. 2005, in Chromospheric and Coronal Magnetic Fields, ed. D. E. Innes, A. Lagg, & S. K. Solanki (ESA SP-596; Noordwijk: ESA), s2_11
Démoulin, P. 2006, Adv. Space Res., 37, 1269
Démoulin, P., Priest, E. R., & Lonie, D. P. 1996, J. Geophys. Res., 101, 7631
Forbes, T. G., & Priest, E. R. 1995, ApJ, 446, 377
Galsgaard, K., Titov, V. S., & Neukirch, T. 2003, ApJ, 595, 506
Harvey, K. L., & Zwaan, C. 1993, Sol. Phys., 148, 85
Haynes, A. L., & Parnell, C. E. 2007, Phys. Plasmas, 14, 082107
Haynes, A. L., Parnell, C. E., Galsgaard, K., & Priest, E. R. 2007, Proc. R. Soc. Ser. A, 463, 1097
Henney, C. J., & Harvey, J. W. 2001, AGU Spring Meeting Abstracts, 51
Hornig, G., & Priest, E. 2003, Phys. Plasmas, 10, 2712
Howard, T. A., Nandy, D., & Koepke, A. C. 2008, J. Geophys. Res. (Space Phys.), 113, 1104
Jackson, J. D. 1962, Classical Electrodynamics (New York: Wiley)
Klimchuk, J. A. 2001, in Geophysical Monograph 125, Space Weather, ed. P. Song, H. Singer, & G. Siscoe (Washington, DC: AGU), 143
Kusano, K., Maeshiro, T., Yokoyama, T., & Sakurai, T. 2004, ApJ, 610, 537
Lin, J., Soon, W., & Baliunas, S. L. 2003, New Astron. Rev., 47, 53
Longcope, D. W., & Beveridge, C. 2007, ApJ, 669, 621
Longcope, D. W., Brown, D. S., & Priest, E. R. 2003, Phys. Plasmas, 10, 3321
Longcope, D. W., & Parnell, C. E. 2009, Sol. Phys., 254, 51
Lynch, B. J., Antiochos, S. K., Devore, C. R., & Zurbuchen, T. H. 2004, AGU Fall Meeting Abstracts, 400
Mackay, D. H., Gaizauskas, V., & van Ballegooijen, A. A. 2000, ApJ, 544, 1122
Mackay, D. H., & Lockwood, M. 2002, Sol. Phys., 209, 287
Mackay, D. H., Priest, E. R., & Lockwood, M. 2002, Sol. Phys., 207, 291
Maclean, R., Beveridge, C., Longcope, D., Brown, D. S., & Priest, E. R. 2005, Proc. R. Soc. Ser. A, 461, 2099
Maclean, R. C., Beveridge, C., & Priest, E. R. 2006a, Sol. Phys., 238, 13
Maclean, R. C., Hornig, G., Priest, E. R., & Beveridge, C. 2006b, Sol. Phys., 235, 280
Maclean, R. C., & Priest, E. R. 2007, Sol. Phys., 243, 171
MacNeice, P., Antiochos, S. K., Phillips, A., Spicer, D. S., DeVore, C. R., & Olson, K. 2004, ApJ, 614, 1028
Murray, M. J., & Hood, A. W. 2007, A&A, 470, 709
Murray, M. J., Hood, A. W., Moreno-Insertis, F., Galsgaard, K., & Archontis, V. 2006, A&A, 460, 909
Nandy, D., & Choudhuri, A. R. 2001, ApJ, 551, 576
Pariat, E., Aulanier, G., & Démoulin, P. 2006, SF2A-2006: Semaine de l'Astrophysique Francaise, ed. D. Barret et al. (Paris: French Astron. Soc. Astrophys.), 559
Parnell, C. E., & Galsgaard, K. 2004, A&A, 428, 595
Parnell, C. E., Haynes, A. L., & Galsgaard, K. 2008, ApJ, 675, 1656
Parnell, C. E., Neukirch, T., Smith, J. M., & Priest, E. R. 1997, Geophys. Astrophys. Fluid Dyn., 84, 245
Parnell, C. E., Smith, J. M., Neukirch, T., & Priest, E. R. 1996, Phys. Plasmas, 3, 759
Pierce, A. K., Livingston, W. C., Harvey, J. W., Schrage, D., Gillespie, B., Simmons, J., & Slaughter, C. 1976, Appl. Opt., 15, 33
Pontin, D. I., Hornig, G., & Priest, E. R. 2004, Geophys. Astrophys. Fluid Dyn., 98, 407
Pontin, D. I., Hornig, G., & Priest, E. R. 2005, Geophys. Astrophys. Fluid Dyn., 99, 77
Priest, E. R., & Démoulin, P. 1995, J. Geophys. Res., 100, 23443
Priest, E. R., & Forbes, T. G. 1990, Sol. Phys., 126, 319
Priest, E. R., Hornig, G., & Pontin, D. I. 2003, J. Geophys. Res. (Space Phys.), 108, 1285
Régnier, S., Parnell, C. E., & Haynes, A. L. 2008, A&A, 484, L47
Riley, P., Linker, J. A., Mikić, Z., Lionello, R., Ledvina, S. A., & Luhmann, J. G. 2006, ApJ, 653, 1510
Schatten, K. H., Wilcox, J. M., & Ness, N. F. 1969, Sol. Phys., 6, 442
Schrijver, C. J., & Harvey, K. L. 1994, Sol. Phys., 150, 1
Schrijver, C. J., & Title, A. M. 2001, ApJ, 551, 1099
Schüssler, M., & Baumann, I. 2006, A&A, 459, 945
Snodgrass, H. B. 1983, ApJ, 270, 288
Titov, V. S., Galsgaard, K., & Neukirch, T. 2003, ApJ, 582, 1172
Tokman, M., & Bellan, P. M. 2002, ApJ, 567, 1202
Török, T., & Kliem, B. 2003, A&A, 406, 1043
van Ballegooijen, A. A., Cartledge, N. P., & Priest, E. R. 1998, ApJ, 501, 866
van Ballegooijen, A. A., & Martens, P. C. H. 1989, ApJ, 343, 971
Wang, Y.-M., Nash, A. G., & Sheeley, N. R., Jr. 1989, Science, 245, 712
Yashiro, S., Gopalswamy, N., Michalek, G., St. Cyr, O. C., Plunkett, S. P., Rich, N. B., & Howard, R. A. 2004, J. Geophys. Res. (Space Phys.), 109, 7105
Yeates, A. R., & Mackay, D. H. 2009, ApJ, 699, 1024
Yeates, A. R., Mackay, D. H., & van Ballegooijen, A. A. 2007, Sol. Phys., 245, 87
Yeates, A. R., Mackay, D. H., & van Ballegooijen, A. A. 2008, Sol. Phys., 247, 103
Yeates, A. R., Nandy, D., & Mackay, D. H. 2008, ApJ, 673, 544
Zhang, J., Woch, J., Solanki, S. K., & von Steiger, R. 2002, EGS XXVII General Assembly, Nice, 21–26 April, abstract 4034